



## Fire Resistance of Crushed Brick-Based Alkali-Activated Mortars

Dalibor Kramarić <sup>1\*</sup>, Ivanka N. Grubeša <sup>1</sup>, Neno Torić <sup>2</sup>, Rosana Ribić <sup>1</sup>,  
Nevenka Mijatović <sup>3</sup>, Milica V. Vasić <sup>3</sup>

<sup>1</sup> Department of Civil Engineering, University North, Jurja Križanića 31b, 42000 Varaždin, Croatia.

<sup>2</sup> Faculty of Civil Engineering, Architecture and Geodesy, University of Split, 21000 Split, Croatia.

<sup>3</sup> Centre for Materials, Institute for Testing of Materials IMS, Bulevar Vojvode Mišića 43, 11000 Belgrade, Serbia.

Received 26 November 2024; Revised 11 March 2025; Accepted 18 March 2025; Published 01 April 2025

### Abstract

This study investigates the fire resistance of alkali-activated mortar incorporating crushed brick as both a precursor and aggregate. The optimal alkaline activator was identified as a combination of KOH and Na<sub>2</sub> SiO<sub>3</sub>, with a curing period of 3 days at 70 °C. Two mortar series were produced, each exhibiting different workability: one series comprised cement mortar, while the other included three alkali-activated mortars, with variations in the molarity of the KOH solution. The mortar samples were subsequently heated to 600°C, and their mechanical properties and mass were measured to determine residual values/losses. The best-performing alkali-activated and cement mortars underwent visual assessments of cross-sections to evaluate the impact of mortar consistency on fire resistance. Additionally, changes in mineralogy and microstructure were followed by instrumental techniques to clarify the results before and after heating. While cement mortars had superior mechanical properties at room temperature, alkali-activated mortars retained a higher percentage of their mechanical properties post-heating, demonstrating better fire resistance. Mortars with plastic consistency showed better fire resistance than those with fluid consistency. These findings suggest that brick-based alkali-activated mortars could be developed into fire protection boards for structural members.

**Keywords:** Alkali-Activated Mortar; Fire Resistance; Mechanical Properties; Mass; FT-IR; FE-SEM-EDS Analysis.

## 1. Introduction

The durability of a structure is essential for building materials, with fire resistance being a key aspect of the durability. When it comes to concrete, while it is non-combustible, its properties deteriorate when exposed to high temperatures [1]. The extent of concrete degradation is typically measured by the residual mechanical properties, particularly compressive strength. The performance of concrete at elevated temperatures is influenced by its composition and the compatibility of its components. Specifically, the binder, usually cement, tends to contract at high temperatures, while aggregate expands, resulting in the formation of cracks in the interfacial transition zone (ITZ) between the aggregate and the paste [2]. Therefore, it is vital to select a binder and aggregate that exhibit similar thermal behavior when exposed to fire.

As an alternative to conventional concrete, alkali-activated binders have garnered increasing attention due to their superior performance under high-temperature conditions [3-5]. These binders are created by treating aluminosilicate materials, known as precursors, with an alkaline activator in conjunction with a Na-silicate solution [6]. Various materials can serve as precursors: a) natural resources like kaolin, which is processed into metakaolin; b) industrial by-

\* Corresponding author: [dakramaric@unin.hr](mailto:dakramaric@unin.hr)

<http://dx.doi.org/10.28991/CEJ-2025-011-04-05>



© 2025 by the authors. Licensee C.E.J, Tehran, Iran. This article is an open access article distributed under the terms and conditions of the Creative Commons Attribution (CC-BY) license (<http://creativecommons.org/licenses/by/4.0/>).

products such as fly ash and slag; and c) construction waste, including rubble from demolished buildings—whether from targeted demolition or earthquake damage—and low-quality bricks produced in the brick manufacturing sector. The incorporation of waste materials and construction debris in the production of alkali-activated materials is particularly significant, as it aids in conserving natural resources [7], managing waste [8, 9], saving energy [10, 11], and reducing CO<sub>2</sub> emissions [9-12] during cement production. The literature identifies several commonly used alkaline activators, including NaOH, KOH, Na<sub>2</sub>SiO<sub>3</sub>, K<sub>2</sub>SiO<sub>3</sub>, Na<sub>2</sub>CO<sub>3</sub>, CaO, and Ca(OH)<sub>2</sub>, along with their various combinations [13].

When the precursor has a high concentration of CaO, a C-A-S-H gel forms during the hardening process [14, 15]. Conversely, a precursor with a low CaO content but rich in aluminosilicates will yield an N-A-S-H gel [14, 16]. The fire resistance of alkali-activated binders is significantly enhanced at high temperatures when utilizing N-A-S-H and C-A-S-H gels, especially in comparison to Portland cement. Notably, the primary hydration products of Portland cement, C-S-H, decompose at temperatures of 150 °C and 450 °C, ultimately disintegrating at 740 °C [14]. In contrast, N-A-S-H and C-A-S-H gels maintain their stability at temperatures reaching 700-800 °C [14]. Literature indicates that alkali-activated binders preserve favorable mechanical properties after fire exposure, with resilience noted at temperatures of 550, 600, and even up to 1200 °C [17-21]. Research conducted by Duan et al. [22] reveals that Portland cement loses all its strength at 600 °C, whereas the alkali-activated binder retains 75% of its initial strength even at 1000 °C. Furthermore, these researchers found that alkali-activated paste contracts significantly less at elevated temperatures compared to cement paste, potentially making it more suitable for integration with aggregates in composites that expand as the temperatures rise.

According to Song et al. [23], the N-A-S-H gel demonstrates greater stability at high temperatures compared to C-A-S-H gel, which shares properties similar to those of cement. The precursors most likely to form N-A-S-H gel upon alkaline activation are metakaolin, low-CaO fly ash, and crushed brick in powdered form. Crushed brick is considered construction waste and can be generated from the demolition of masonry structures due to natural events or earthquakes, followed by a crushing process. Additionally, this powder may originate from brick manufacturing facilities, where brick elements are ground to achieve flatness or crushed if they fail to meet the required quality standards for market placement.

Previous studies have mainly focused on the properties of alkali-activated binders using crushed brick as a precursor at the paste level. Table 1 presents the input parameters, and the resulting mechanical properties observed in research conducted on alkali-activated paste levels.

**Table 1. Overview of previous research utilizing crushed brick as a precursor in alkali-activated paste**

Research	Precursor	Alkaline activator	Curing regime	Achieved mechanical properties at the age of 28 days (MPa)
Gado et al. (2020) [24]	Crushed brick	NaOH+Na <sub>2</sub> SiO <sub>3</sub>	Room temperature	Compressive strength of 32 MPa
Cardoza & Colorado (2023) [25]	Crushed brick	NaOH+Na <sub>2</sub> SiO <sub>3</sub>	Room temperature	Compressive strength of 33.11 MPa and flexural strength of 13.8 MPa
García-Díaz et al. (2024) [26]	A mix of construction waste and crushed brick	NaOH+Na <sub>2</sub> SiO <sub>3</sub>	Room temperature	Compressive strength of 29.7 MPa and flexural strength of 15.7 MPa for a mix of construction waste to the crushed brick ratio of 60:40
Statkaustas et al. (2023) [16]	Mix of crushed brick and metakaolin, with a small amount of phosphogypsum	NaOH	24h at room temperature, 24 h at 60 °C, and the rest of the time at room temperature	Compressive strength of 35.1 MPa for a mix of crushed brick to metakaolin of 70:30
Robayo et al. (2016) [27]	Crushed brick;	NaOH+Na <sub>2</sub> SiO <sub>3</sub>	24h at room temperature; 24 h/48 h at 70 °C, the rest of the time at room temperature	Compressive strength of 16.36 MPa for 48 h of oven curing at 70 °C, the rest of the time at room temperature
	Mix of crushed brick and Portland cement	NaOH+Na <sub>2</sub> SiO <sub>3</sub>	At room temperature	Compressive strength of 102.6 MPa for a mix of crushed brick to Portland cement of 80:20
Robayo-Salazar et al. (2017) [28]	Mix of crushed brick and Portland cement	Na <sub>2</sub> SO <sub>4</sub> , Na <sub>2</sub> CO <sub>3</sub> , NaOH, NaOH+Na <sub>2</sub> SiO <sub>3</sub>	At room temperature	Compressive strength of 102 MPa for a mix of crushed brick to Portland cement of 80:20 and alkaline activator NaOH+Na <sub>2</sub> SiO <sub>3</sub>
Zhang et al. (2021) [29]	Crushed brick	NaOH+Na <sub>2</sub> SiO <sub>3</sub>	0/24h/48h/72h/96h at 50°C, 24 h at 200 °C, the rest of the time at room temperature	Compressive strength of 48 MPa for 48 h at 50 °C and 24h at 200°C (tested directly after curing)
Ulugöl et al. (2021) [30]	Crushed brick	NaOH	24h/48h/72h at 50/66/75/85, 95/105/115/125 °C	Compressive strength of 45.7 MPa for 24 h at 105 °C (tested directly after curing)
Yildirim et al. (2021) [31]	Crushed brick	NaOH	24h/48h/72h at 95/105/115/125 °C	Compressive strength of 80 MPa for 48 h at 115 °C (tested directly after curing)
Sedira et al. (2018) [11]	A mix of crushed brick and tungsten mining waste mud	NaOH+Na <sub>2</sub> SiO <sub>3</sub>	24h at 60 °C, the rest of the time at room temperature	Compressive strength of 59 MPa for a mix of crushed brick to tungsten mining waste mud of 50:50
Vasić et al. (2022) [32]	A mix of crushed brick and low illitic clay	KOH+Na <sub>2</sub> SiO <sub>3</sub>	- 24h in moisture, 72h in air, and 48h at 60 °C, the rest of the time at room temperature; - 24h in moisture, 72h in air, and 96h at 70 °C, the rest of the time at room temperature; - 24h in moisture, 3 h in steam, 48h in air, and 96h at 70 °C, the rest of time at room temperature.	Flexural strength of 13.7 MPa for 24h in moisture, 3 h in steam, 48h in air, and 96h at 70 °C, the rest of the time at room temperature

Research on the use of crushed brick as a precursor in mortars is notably limited. Reig et al. [33] explored this by utilizing crushed brick alongside quartz sand as an aggregate to create alkali-activated mortars. These mortars were subjected to curing at 65 °C for either 3 or 7 days, achieving commendable compressive strengths, reaching 50 MPa after 7 days of curing. Tuyan et al. [34] developed alkali-activated mortars using crushed brick and quartz sand, curing them at both room temperature and elevated temperatures (ranging from 50 to 100°C) for varying durations from 1 to 7 days. As expected, increased curing temperatures and extended curing times led to enhanced compressive strength values. While there is existing research on the fire resistance of alkali-activated binders, the authors have identified a significant gap in studies specifically addressing the fire resistance of alkali-activated mortars derived from crushed brick.

Most research on the alkali activation of crushed brick predominantly employs sodium-based alkaline activators; a combination of NaOH and Na<sub>2</sub> SiO<sub>3</sub> [11, 24-27, 29, 33, 34] or solely NaOH [16, 30, 31]. In contrast, Robayo-Salazar et al. [28] explored various activators, including Na<sub>2</sub>SO<sub>4</sub>, Na<sub>2</sub>CO<sub>3</sub>, and NaOH – Na<sub>2</sub>SiO<sub>3</sub>. Meanwhile, Vasić et al. [32] utilized a blend of KOH and Na<sub>2</sub> SiO<sub>3</sub>, achieving impressive flexural strength values with appropriate care. Hosan et al. [35] conducted research on alkali-activated fly ash using a potassium-based alkaline activator, specifically a combination of KOH and K<sub>2</sub>SiO<sub>3</sub>, which exhibited superior fire-resistant properties compared to sodium-based alkali-activated binders (a combination of NaOH and Na<sub>2</sub>SiO<sub>3</sub>). Specifically, while the compressive strengths of pastes activated with sodium-based activators diminished after exposure to 200 °C, those activated with potassium-based activators increased within the 200-600 °C range. Additionally, mass loss, shrinkage, and crack formation during exposure to high temperatures were less pronounced in pastes activated with potassium-based counterparts compared to those activated with sodium-based activators. The enhanced performance may be attributed to the more porous structure of potassium-activated pastes, which facilitates moisture evaporation and mitigates pore pressure buildup at elevated temperatures, thereby protecting the samples from damage [36, 37]. Ghazy et al. [4] investigated the impact of various alkaline activators—sodium (NaOH + Na<sub>2</sub>SiO<sub>3</sub>), potassium (KOH + K<sub>2</sub>SiO<sub>3</sub>), and a combination of both (KOH + Na<sub>2</sub>SiO<sub>3</sub>)—on the fire resistance of alkaline-activated mortars using fly ash as a precursor. Their findings revealed that mortars activated with a combined alkaline activator (KOH + Na<sub>2</sub>SiO<sub>3</sub>) exhibited superior mechanical properties after exposure to temperatures up to 800 °C compared to those activated with either sodium- or potassium-based activators alone. Further, mortars activated with a potassium-based alkaline activator demonstrated better fire resistance than those activated with a sodium-based alkaline activator. Finally, all alkali-activated mortars studied by this group of authors exhibited superior fire resistance compared to Portland cement mortar. Lahoti et al. [38] also studied the impact of different activators on the fire resistance of alkali-activated fly ash paste, including sodium-based (NaOH + Na<sub>2</sub>SiO<sub>3</sub>), potassium-based (KOH + K<sub>2</sub>SiO<sub>3</sub>), and a mixture of sodium- and potassium-based (NaOH + KOH + K<sub>2</sub>SiO<sub>3</sub>) alkaline activators.

Their observations even indicate an increase in compressive strength and minimal internal damage (cracks) in the mortar with a potassium-based alkaline activator after exposure to 600 °C. The mortar with a mixture of sodium- and potassium-based alkaline activators retained its compressive strength but exhibited more significant internal damage, while the mortar with the sodium-based alkaline activator showed a slight decrease in compressive strength and the most noticeable internal damage after exposure to 600 °C. Interestingly, the internal damage (cracks) present in all samples of the alkaline-activated mortars after their exposure to 600 °C disappeared completely after being exposed to 900 °C.

However, it is important to highlight that Ghazy et al. [4] and Lahoti et al. [38] reached their conclusions regarding the superior performance of alkali-activated composites by utilizing a combination of sodium and potassium as the alkaline activator, particularly in studies centered on fly ash-based composites. Additionally, while Vasić et al. [32] showcased the potential for achieving commendable mechanical properties in alkali-activated composites made from crushed brick and activated with a blend of potassium hydroxide and sodium silicate, the fire resistance of such composites remains unexamined.

Clay brick masonry is one of the oldest and most durable construction methods used by humans [39]. However, many existing masonry buildings have lost their functionality and need to be demolished to make way for new structures. These buildings often collapse due to earthquakes, and whether removed due to deterioration or earthquake damage, significant amounts of waste are generated. Additionally, the clay brick industry produces large quantities of brick dust during the grinding of brick units to achieve the required flatness. Furthermore, some brick units are deemed unsuitable for market use due to defects such as cracks or poor quality and are subsequently discarded in landfills near the manufacturing site. Regardless of how this waste is generated, there is potential to repurpose it with an added value. This paper investigates the possibility of utilizing crushed brick waste in alkali-activated mortars, intending to help protect buildings from the high temperatures developed during a fire.

## 2. Experimental Part

The characterization of all materials used for mortar production (cement - CEM, brick powder - BP, aggregate from crushed brick products/crushed brick aggregate - CBA) was conducted through chemical analysis, laser diffraction, and Fourier-transform infrared spectroscopy (FT-IR).

To evaluate the compatibility of brick powder (BP) as a precursor with alkaline components (KOH/ a combination of KOH and  $\text{Na}_2\text{SiO}_3$ ), a screening test was conducted on samples with simple preparation, leading to the selection of the optimal alkaline activator and the appropriate curing method for alkali-activated samples. Subsequently, two series of mortars with different workability were produced, with cement mortar and three alkali-activated mortars within each series, in which the molarity of the KOH solution, a component of the alkaline activator, was varied. A total of eight mortar mixtures were prepared and tested for consistency in the fresh state, mechanical properties at room temperature, and after exposure to high temperatures. For the alkali-activated mortar and cement mortars that exhibited the best mechanical properties after exposure to high temperatures in each group, a visual assessment of the cross-sections was conducted to evaluate the impact of the mortar's consistency on its fire resistance. For the alkali-activated mortar that retained the best mechanical properties after exposure to high temperatures among all the alkali-activated mortars, as well as the cement mortar of the same workability, FT-IR spectra and Field Emission Scanning Electron Microscopy equipped with Energy Dispersive Spectroscopy (FE-SEM-EDS) analyses were performed to clarify the previously obtained results before and after exposure to high temperatures. The testing scheme for alkali-activated mixtures is illustrated in Figure 1.

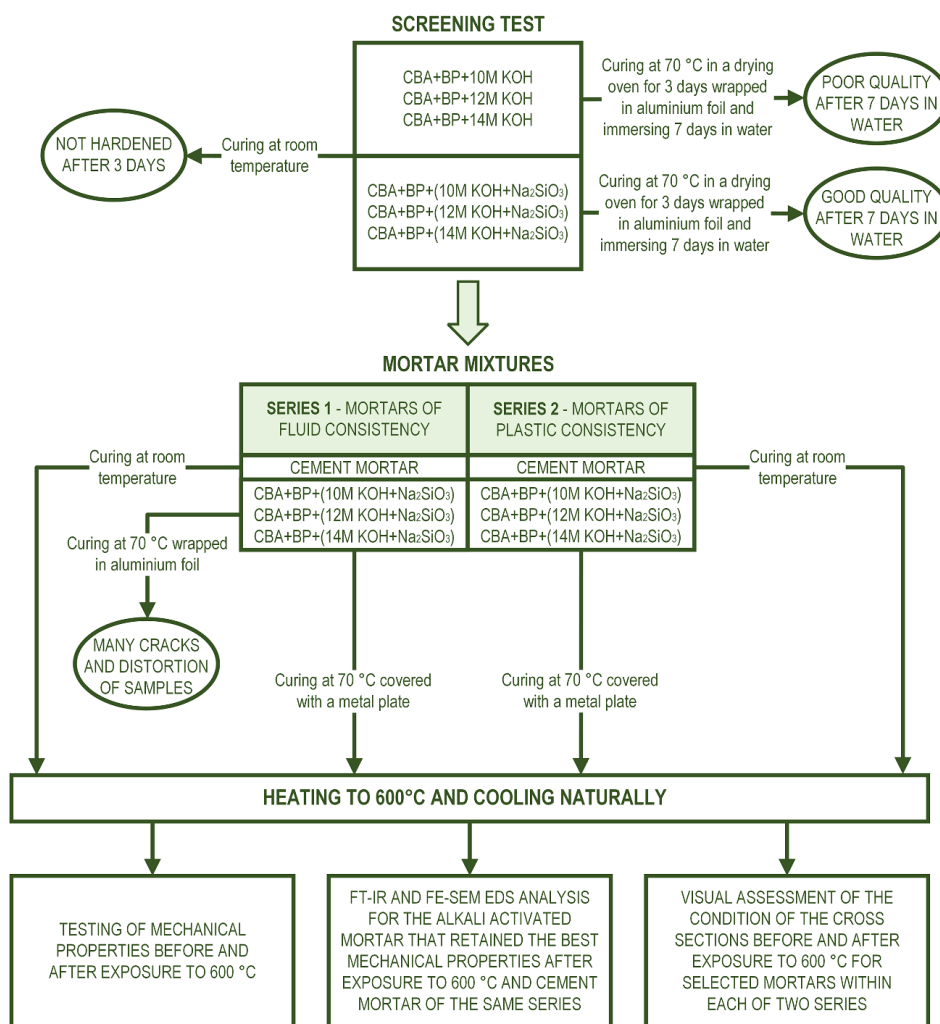


Figure 1. Testing scheme for alkali-activated mixtures

## 2.1. Materials and methods

### 2.1.1. Properties of Aggregate, Binder and Alkaline Activator

The aggregate (CBA) was obtained by crushing brick wall elements produced in a brick manufacturing plant in Turčin, Croatia, which were deemed to be of unsatisfactory quality and therefore were not placed on the market but were considered waste in the production process. In the reference mortar mixture, CEM I 52.5 R cement (CEM) was used as the binder, while in the alkali-activated mortar mixtures, brick powder (BP) obtained from grinding bricks in the Cerje Tužno brick factory (Croatia) was used as a precursor.

Figure 2 shows the appearance of the crushed brick aggregate (CBA), brick powder (BP), and cement (CEM) captured by a digital camera at 60x magnification.

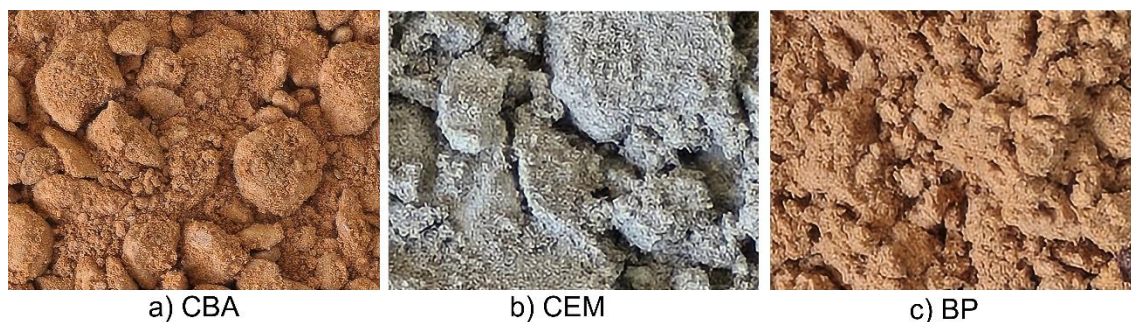


Figure 2. Appearance of a) crushed brick aggregate (CBA), b) cement (CEM) and c) brick powder (BP) captured by a digital camera at 60x magnification

The chemical composition of the aggregate, cement, and brick powder was determined using the EDXRF method under EN 196-2:2013 [40]. The granulometric composition of the aggregate, cement, and brick powder was determined using laser diffraction according to ISO 13320:2020 [41]. Fourier-transform infrared spectroscopy (FT-IR) was used to detect minerals present in the initial materials. Thermo Fisher Scientific instrument Nicolet iS10 in the mid-infrared range was employed. The samples were crushed in a pestle with mortar to minimize the noise, dried at 105 °C to constant mass, and immediately measured. An aqueous solution of KOH with molar concentrations of 10 M, 12 M, and 14 M was used as the alkaline activator, along with a mixture of 10 M, 12 M, and 14 M KOH solutions and a sodium silicate ( $\text{Na}_2\text{SiO}_3$ ) solution, where the molar ratio of  $\text{Na}_2\text{SiO}_3$  to KOH was 1:2.5. The KOH solution was obtained by dissolving KOH granules (from the manufacturer Gram-Mol d.o.o.) in water.  $\text{Na}_2\text{SiO}_3$  (from the manufacturer Gram-Mol d.o.o.) was in liquid form.

### 2.1.2. Screening Test

In the screening test, 50 g of brick powder (BP) as a precursor, 150 g of crushed brick aggregate (CBA), and 73 g of aqueous KOH solutions with concentrations of 10 M, 12 M, and 14 M, as well as mixtures of 10 M, 12 M, and 14 M KOH solutions with sodium silicate ( $\text{Na}_2\text{SiO}_3$ ), where the molar ratio of  $\text{Na}_2\text{SiO}_3$  to KOH was 1:2.5, were mixed. The obtained mixtures were poured into molds and cured at room temperature and at 70 °C in a drying oven for 3 days, wrapped in aluminum foil to prevent evaporation of the liquid component (Figure 3).

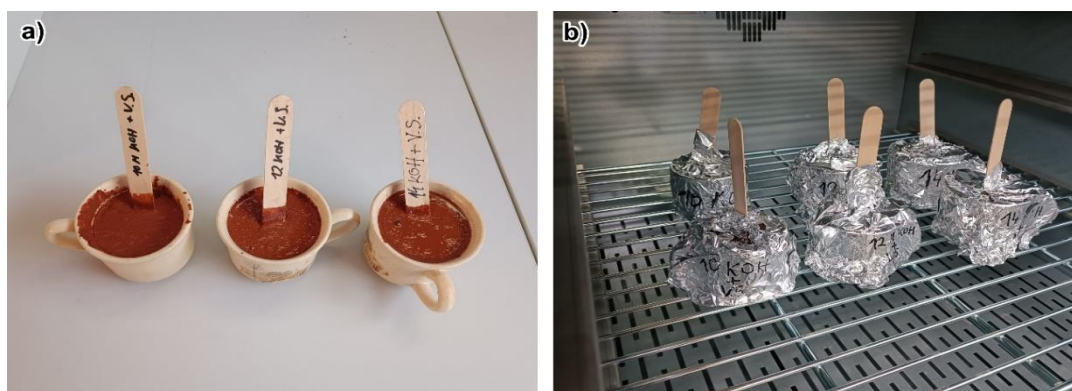


Figure 3. Curing of alkali-activated “lollipops”: a) at room temperature, and b) in a drying oven

All the “lollipops” were subsequently immersed in water (Figure 4) for 7 days to visually assess their water absorption capacity.



Figure 4. Alkali-activated “lollipops” immersed in water

**2.1.3. Testing at the Mortar Scale**

In the mortar scale part of the research, four mortar mixtures were prepared in two different consistencies, plastic and fluid consistencies. Within each consistency, one mixture was a cement mortar, while the remaining three mixtures were alkali-activated mortars. The cement used for making the cement mortars (CEM), the brick powder used as the precursor (BP), and the crushed brick aggregate (CBA) were the same as for the screening test. The alkaline activator was a mixture of 10 M KOH, 12 M KOH and 14 M KOH and a sodium silicate solution (Na<sub>2</sub>SiO<sub>3</sub>) where the molar ratio of Na<sub>2</sub>SiO<sub>3</sub> to KOH was 1:2,5. Details of the mortar mixtures are presented in Table 2. The consistency of the mortars was tested according to EN 1015-3:2005 [42].

**Table 2. Details of the prepared mortar mixtures**

Series	Mixture	Cement, CEM (g)	Brick powder, BP (g)	Aggregate, CBA (g)	Molarity of the solution KOH	KOH solution + Na <sub>2</sub> SiO <sub>3</sub> solution		
						Mass KOH (g)	Mass of water (g)	Mass of solution Na <sub>2</sub> SiO <sub>3</sub> (g)
	R1	750	-	2250	-	-	900	-
A1	A-1-10	-	750	2250	10	264	373	663
	A-1-12	-	750	2250	12	285	306	709
	A-1-14	-	750	2250	14	298	258	744
	R2	750	-	2250	-	-	610	-
A2	A-2-10	-	750	2250	10	224	315	561
	A-2-12	-	750	2250	12	241	259	600
	A-2-14	-	750	2250	14	251	219	630

Mortar mixtures were cast into three-part molds measuring 4x4x16 cm. Mixtures A-1-10, A-1-12, and A-1-14 were cured in the mold at elevated temperature for 3 days, covered with a foil or a 10 mm thick metal plate, while mixtures A-2-10, A-2-12, and A-2-14 were cured at elevated temperature for 3 days, covered with a 10 mm thick metal plate. Sample curing is shown in Figure 5. Cement mortar samples were cured for 1 day in the mold, and then at room temperature.



**Figure 5. Curing of alkali-activated mortar samples at 70 °C for 3 days: a) with coverage by foil and b) with coverage by a metal plate**

**2.1.3.1. The Heating and Cooling Regime of the Mortar Samples**

Samples measuring 4x4x16 cm of cement mortar and alkali-activated mortar cured with metal plate coverage were heated in an electric furnace NABERTHERM L9/11/P330 (Figure 6) at a rate of 4 °C/min, following the RILEM TC 129-MHT [43] guidelines. The temperature was raised to 600 °C and maintained for 60 minutes. This temperature was chosen because it highlights the distinct behavioral differences between cement and alkali-activated binders, as noted by Pan et al. [17, 19], with alkali-activated mortar showing improved mechanical properties, while cement mortar's properties decline [21]. After the heating period, the samples were allowed to cool naturally to room temperature within the furnace.



Figure 6. Samples in the electric furnace

### 2.1.3.2. Testing of the Mortar Samples Before and After being Exposed to High Temperature

Flexural and compressive strength, elasticity moduli, and mass were measured on cement mortar samples and alkali-activated mortar samples cured with metal plate coverage. Measurements were taken for both high temperatures exposed samples and those that were not, aiming to assess the residual values or losses for each property. Flexural and compressive strength of the mortars were determined according to EN 1015-11:2019 [44]. According to the standard's recommendation, flexural strength was determined at a loading rate of 50 N/s, while compressive strength was determined at a loading rate of 400 N/s. Elastic moduli were determined by reading from the linear portion of the stress-strain curves ( $E = \sigma/\epsilon$ ) obtained during the compressive strength testing. The mass was measured on three samples before and after exposure to high temperatures.

For the alkali-activated mortar that retained the best mechanical properties after exposure to high temperatures within each series, as well as for the cement mortars, a visual assessment of the condition of cross-sections was performed to evaluate the effect of mortar consistency on its fire resistance. The appearance of the cross sections was captured by a digital camera at 60x magnification.

For the alkali-activated mortar that retained the best mechanical properties after exposure to high temperatures among all alkali-activated mortars, as well as for the cement mortar with the same workability, FT-IR spectra and Field Emission Scanning Electron Microscopy equipped with Energy Dispersive Spectroscopy (FE-SEM-EDS) analyses were performed to clarify the previously obtained results before and after exposure to high temperatures. The FT-IR spectrum was determined using the same procedure as for the initial materials. Samples cured for 28 days were vacuumed and coated with Au-Pd in a 15 nm layer in the Fisons instruments chamber, and their surface micromorphology and elemental composition were examined by FE-SEM-EDS using the MIRA 3 XMU Tescan instrument. The SEM images were obtained in a high vacuum using magnifications up to 5,000x.

## 2.2. Results and Discussion

### 2.2.1. Results on Initial Materials Level

The results of the chemical composition analysis are presented in Table 3.

Table 3. Chemical composition of aggregates, cement, and brick powder

Material	P <sub>2</sub> O <sub>5</sub>	Na <sub>2</sub> O	K <sub>2</sub> O	CaO	MgO	Al <sub>2</sub> O <sub>3</sub>	TiO <sub>2</sub>	Fe <sub>2</sub> O <sub>3</sub>	SiO <sub>2</sub>	MnO <sub>2</sub>	SO <sub>3</sub>	Loss on ignition (%)
Crushed brick aggregate (CBA)	0.15	0.66	3.08	1.80	2.31	18.49	1.33	7.72	62.53	0.09	0.45	1.37
Cement (CEM)	0.06	0.27	0.80	63.82	1.29	4.66	0.20	2.56	20.34	0.04	2.70	3.10
Brick powder (BP)	0.14	0.56	3.39	1.59	2.05	17.82	1.42	8.14	63.71	0.12	0.08	0.99

The granulometric composition of the aggregate, cement, and brick powder are presented in Table 4 and Figure 7.

**Table 4. Particle size distribution parameters**

Material	Parameters					
	D <sub>10</sub> (μm)	D <sub>50</sub> (μm)	D <sub>90</sub> (μm)	D <sub>mean</sub> (μm)	D <sub>modal</sub> (μm)	Distribution range
Crushed brick aggregate (CBA)	0.15	0.66	3.08	0.09	0.45	1.37
Cement (CEM)	0.06	0.27	0.80	0.04	2.70	3.10
Brick powder (BP)	0.14	0.56	3.39	0.12	0.08	0.99

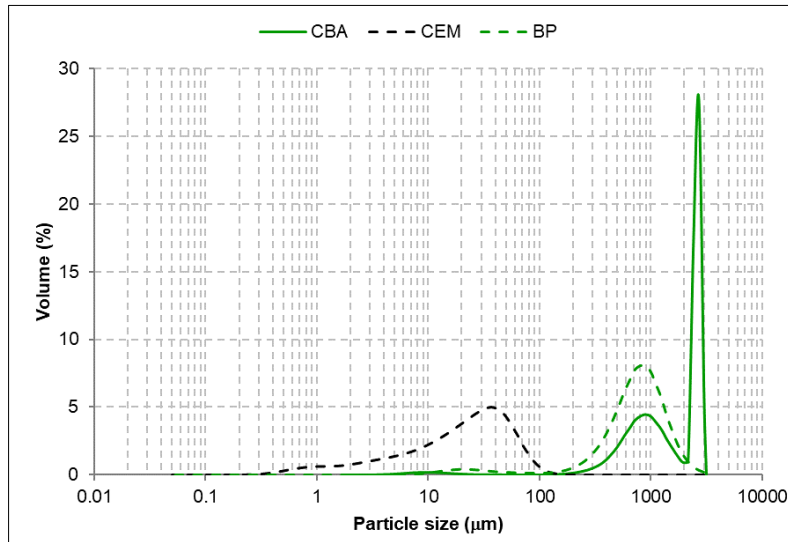


**Figure 7. Particle size distribution**

FT-IR spectra for the initial materials are presented in Figure 8.

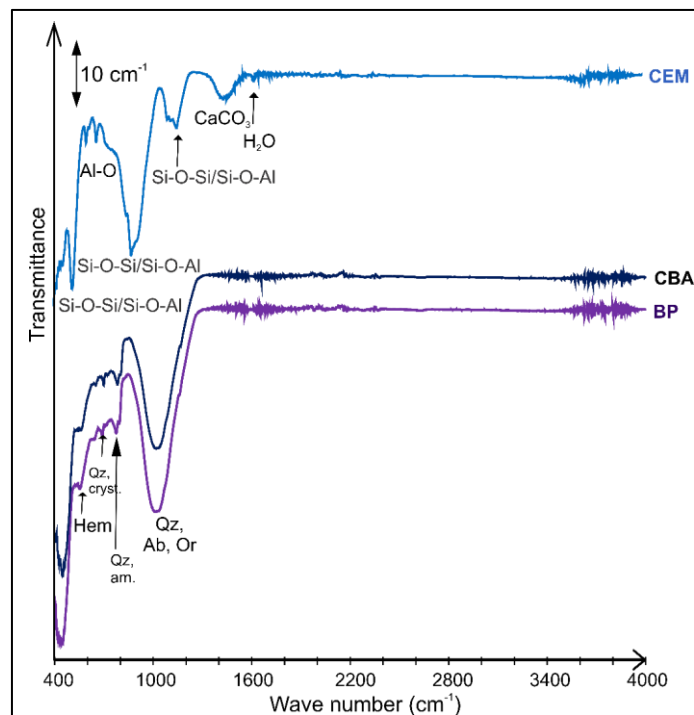


**Figure 8. FT-IR spectra of the initial materials (Qz – quartz, Ab – albite, Or – orthoclase, Hem. – hematite; Qz,cryst. – crystalline quartz, Qz, am. – amorphous quartz)**

**2.2.2. Results of Screening Test**

Alkali-activated mixtures cured at room temperature were of poor quality after 3 days, whereas the alkali-activated mixtures cured at 70 °C did harden properly. The appearance of the alkali-activated 'lollipops' resulting from curing at elevated temperatures is shown in Figure 9.



Figure 9. Appearance of alkali-activated “lollipops” cured at elevated temperature

The result of immersing the alkali-activated “lollipops” in water is shown in Figure 10. Since “lollipops” prepared with KOH disintegrated in water, those alkali-activated mixtures were excluded from further investigation.



Figure 10. Alkali-activated “lollipops” after 7 days in water

### 2.2.3. Results of Testing at the Mortar Scale

Figure 11 shows the appearance of the mixtures during the consistency testing, while Table 5 presents the obtained results of consistency testing.



Figure 11. Consistency testing of mortar mixtures: a) plastic consistency and b) fluid consistency

**Table 5. Results of the mortar consistency testing**

Series	A1				A2			
Mixture	R1	A-1-10	A-1-12	A-1-14	R2	A-2-10	A-2-12	A-2-14
Consistency (cm)	>30	>30	>30	>30	16.0	16.5	23.0	20.0

The appearance of the alkali-activated mortar samples from series A1 after curing is shown in Figure 12.

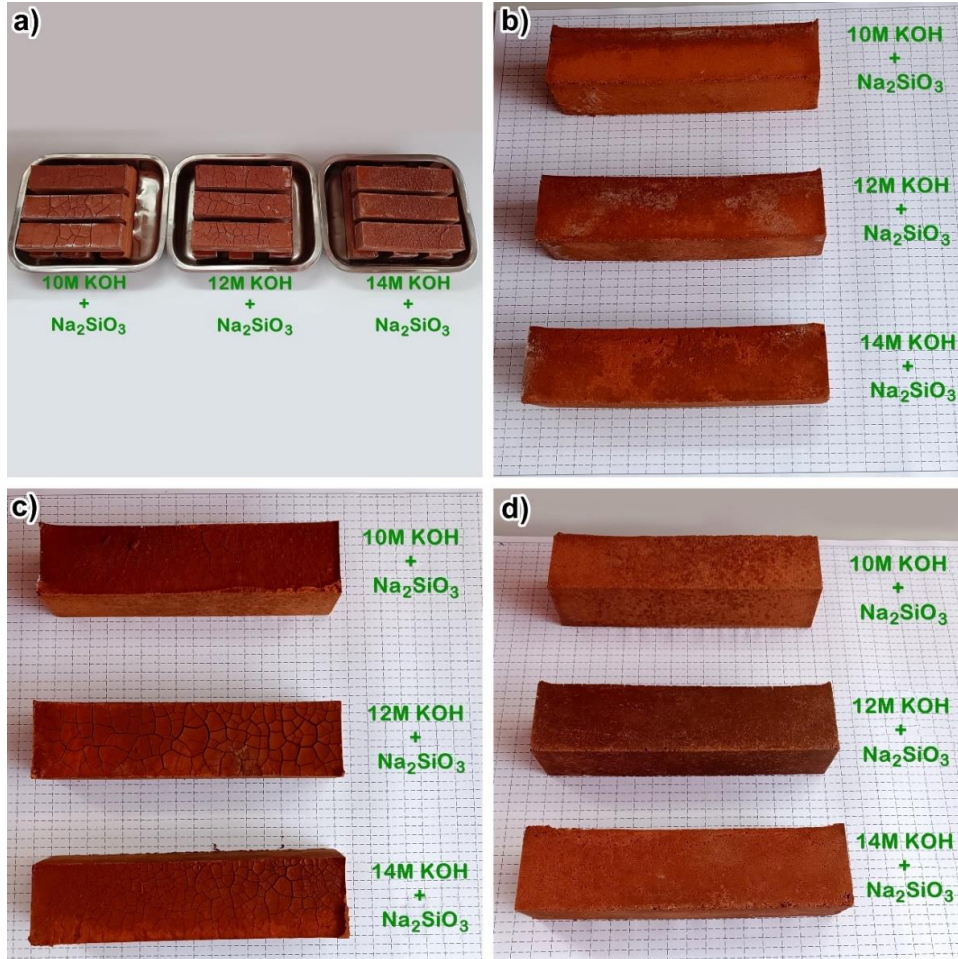


Figure 12. The appearance of alkali-activated mortar samples from series A1: a) surface cracks with curing under foil coverage, b) distortion of samples with curing under foil coverage, c) surface cracks with curing under metal plate coverage and d) distortion of samples with curing under metal plate coverage.

The appearance of the alkali-activated mortar samples from series A2 after curing is shown in Figure 13.

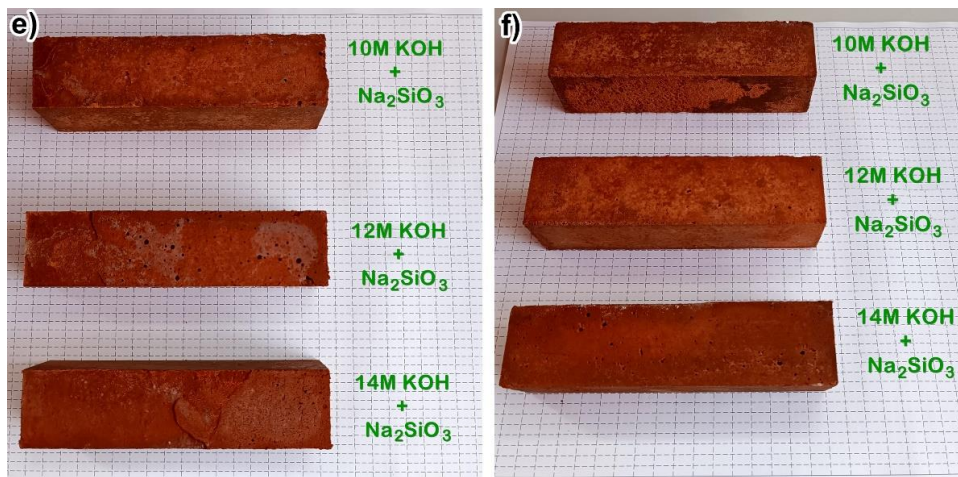


Figure 13. The appearance of alkali-activated mortar samples from series A2: e) surface cracks with curing under metal plate coverage and f) distortion of samples with curing under metal plate coverage

The flexural strength test results are presented in two figures: Figure 14 shows the absolute values, and Figure 15 shows the relative values. Similarly, the compressive strength test results are shown in Figure 16 for absolute values and Figure 17 for relative values. Absolute values include standard deviation and are based on three samples, while relative values are calculated as the ratio of the property of samples exposed to high temperatures to the same property of samples at room temperature. In the presented results, the “A” mark at the end of the name indicates the samples exposed to high temperatures.

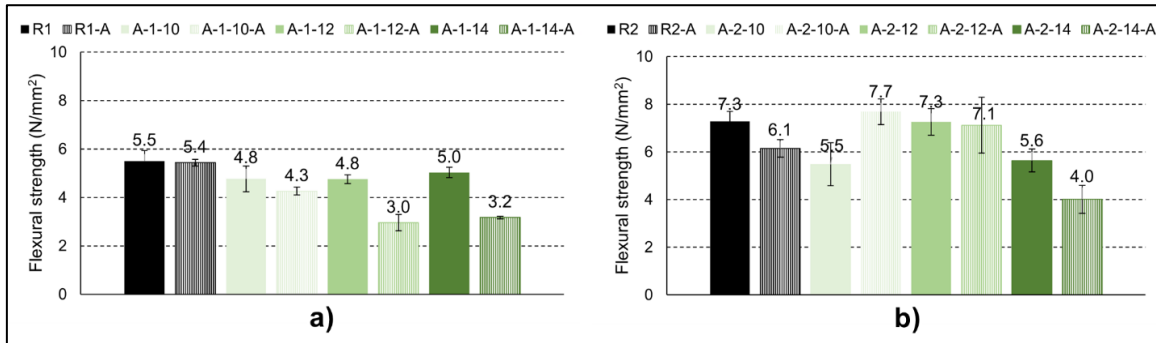


Figure 14. Absolute values of flexural strength of mortars: a) mortars of series A1 (fluid consistency) and b) mortars of series A2 (plastic consistency)

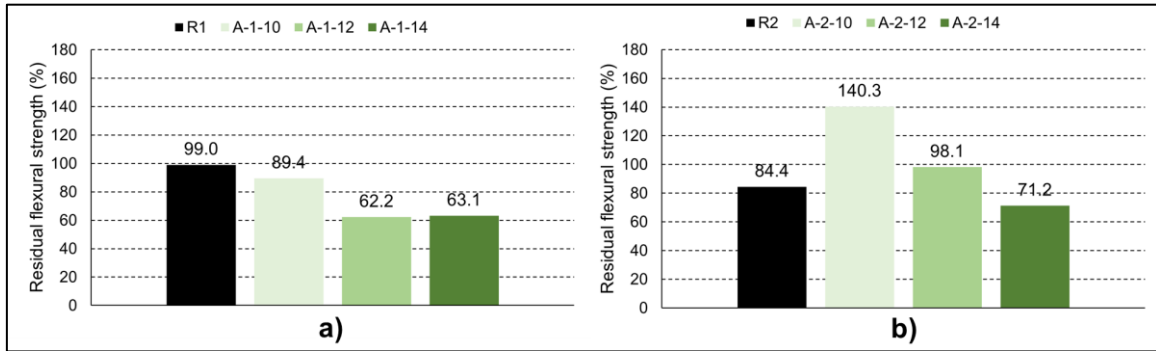


Figure 15. Relative values of flexural strength of mortars: a) mortars of series A1 (fluid consistency) and b) mortars of series A2 (plastic consistency)

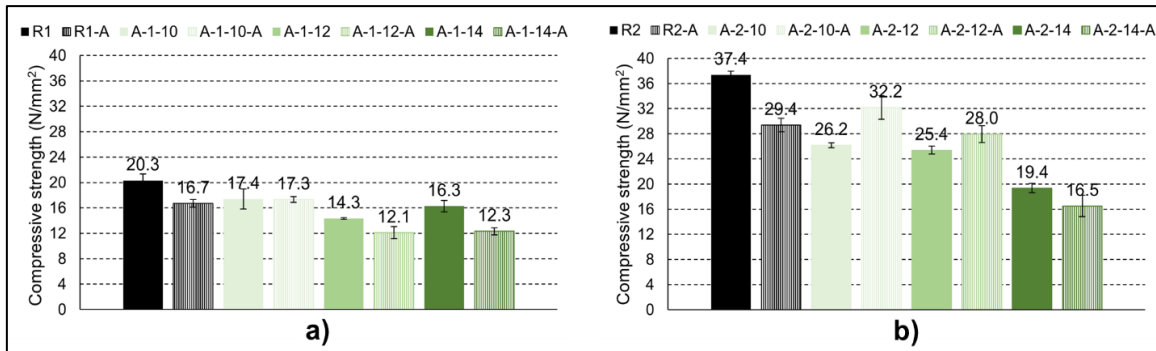


Figure 16. Absolute values of compressive strength of mortars: a) mortars of series A1 (fluid consistency) and b) mortars of series A2 (plastic consistency)

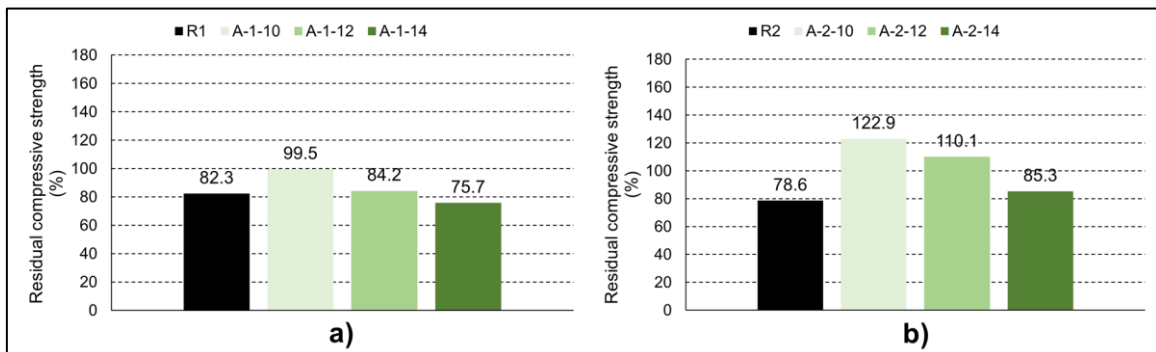


Figure 17. Relative values of compressive strength of mortars: a) mortars of series A1 (fluid consistency) and b) mortars of series A2 (plastic consistency)

Elastic moduli are shown in relative and absolute values (Figures 18 and 19).

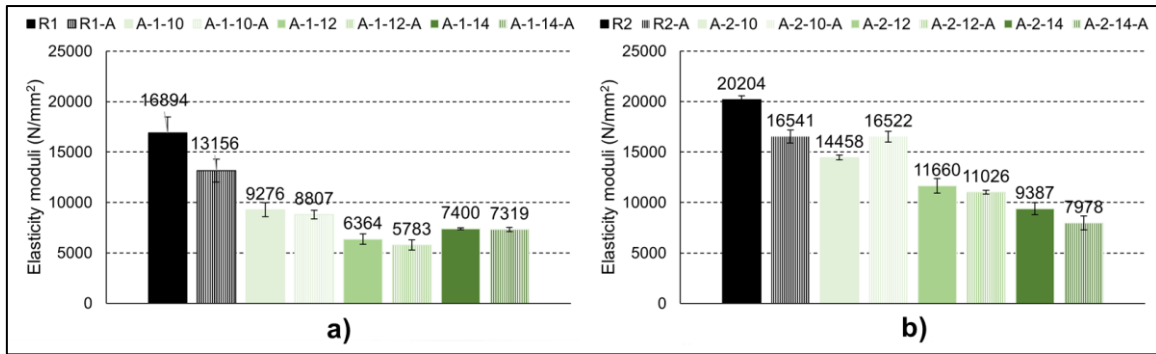


Figure 18. Absolute values of the elastic moduli of the mortars: a) mortars of series A1 (fluid consistency) and b) mortars of series A2 (plastic consistency)

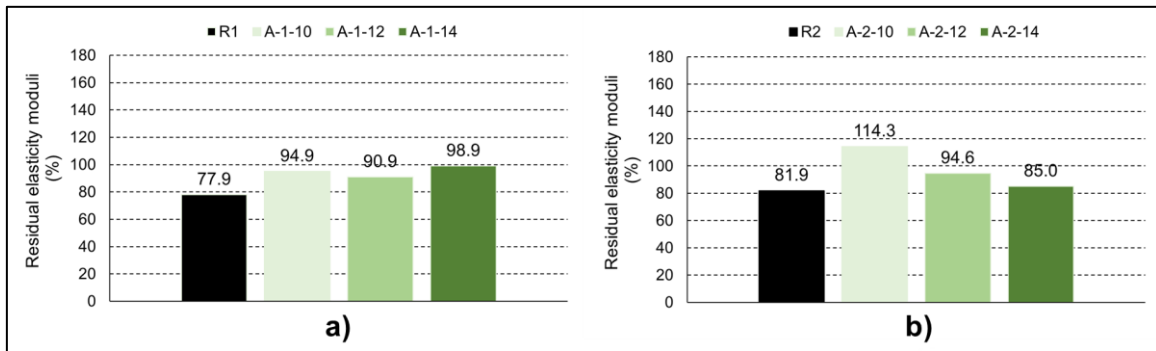


Figure 19. Relative values of the elastic moduli of the mortars: a) mortars of series A1 (fluid consistency) and b) mortars of series A2 (plastic consistency)

The mass losses are shown in Figure 20.

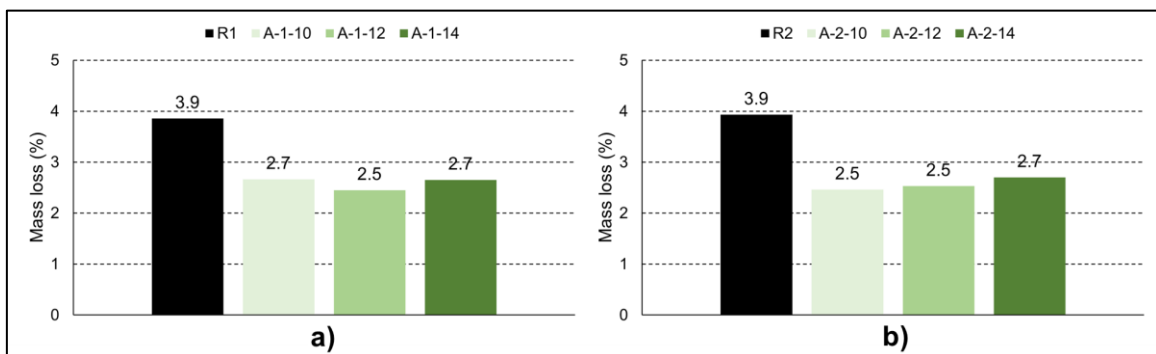
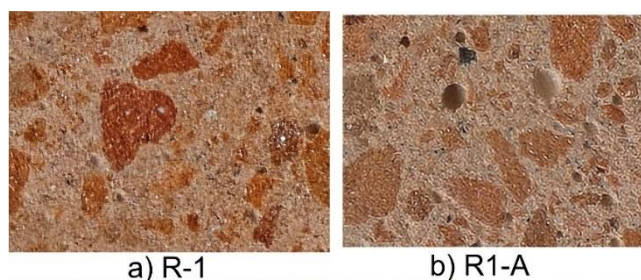


Figure 20. Absolute mass values of the mortars: a) mortars of series A1 (fluid consistency) and b) Mortars of series A2 (plastic consistency)

The appearance of the cross sections, captured by a digital camera at 60x magnification, of the alkali-activated mortar that exhibited the best mechanical properties after exposure to high temperature within each mortar series (mortars A-1-10 and A-2-10) and the cement mortars from both series (mortars R1 and R2), before and after their exposure to high temperature, is shown in Figure 21.



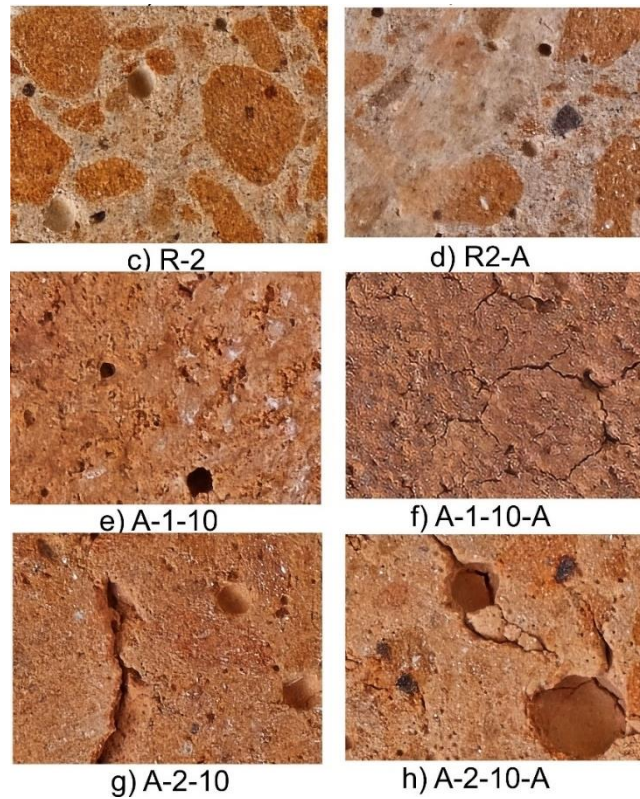


Figure 21. The appearance of the cross-sections of the mortar samples: a) R1, b) R1-A, c) R2, d) R2-A, e) A-1-10, f) A-1-10-A, g) A-2-10 and h) A-2-10-A captured by a digital camera at 60x magnification

The FT-IR spectra of the alkali-activated mortar, which demonstrated the most favourable mechanical properties following exposure to high temperatures (mortar A-2-10), alongside the cement mortar of comparable workability (R2), are presented in Figure 22. Notably, the band associated with  $\text{CaCO}_3$  is absent after the high-temperature exposure.

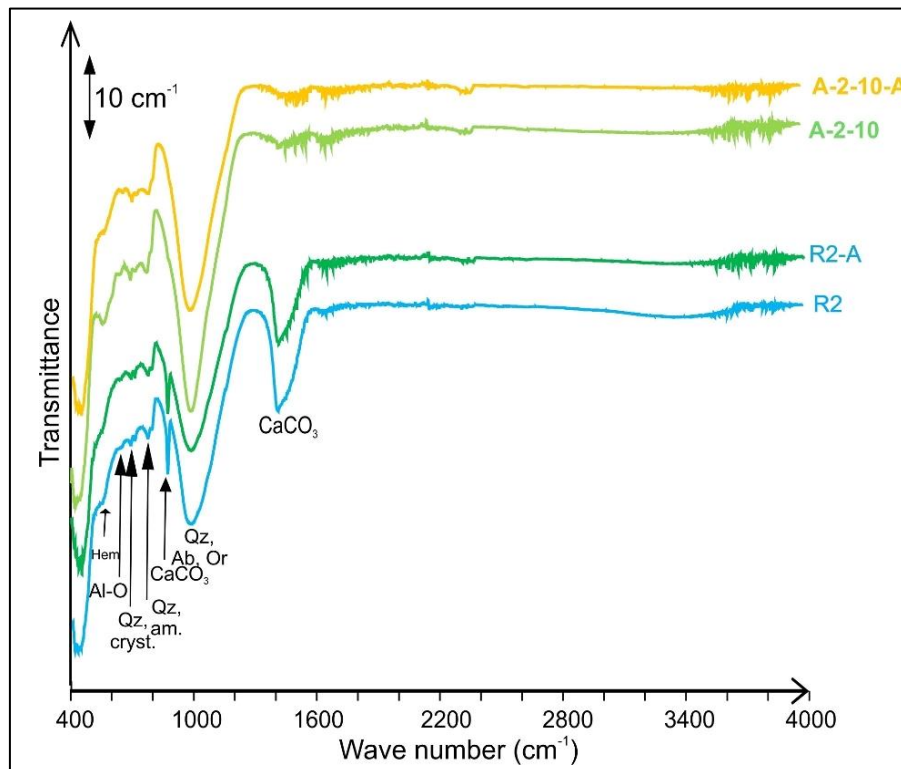


Figure 22. FT-IR spectra of the alkali-activated mortars (Qz – quartz, Ab – albite, Or – orthoclase, Hem. – hematite; Qz,cryst. – crystalline quartz, Qz, am. – amorphous quartz)

FE-SEM-EDS analysis of the alkali-activated mortar, which exhibited the best mechanical properties after exposure to high temperatures (mortar A-2-10), and the cement mortar of similar workability (R2), both before and after exposure to high temperatures, is shown in Figures 23 and 24. The detection of the elemental composition is presented in Tables 6 and 7.

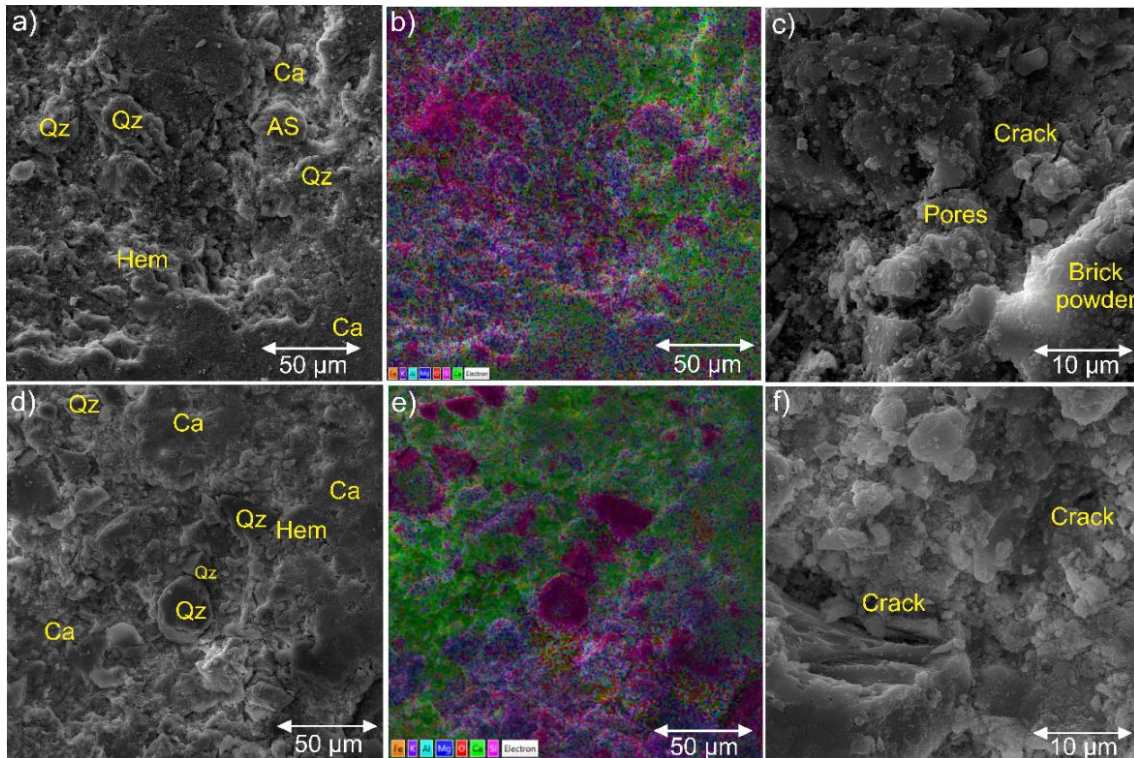


Figure 23. FE-SEM micrographs magnified to 1,000x (with EDS layered image) and 5,000x (50 µm and 10 µm). R2 (a, b, and c) and R2-A (d, e, and f). The used symbols are Qz – Quartz grains, AS – Aluminium silicate phase, Ca – calcium-bearing phase, and Hem – Hematit.

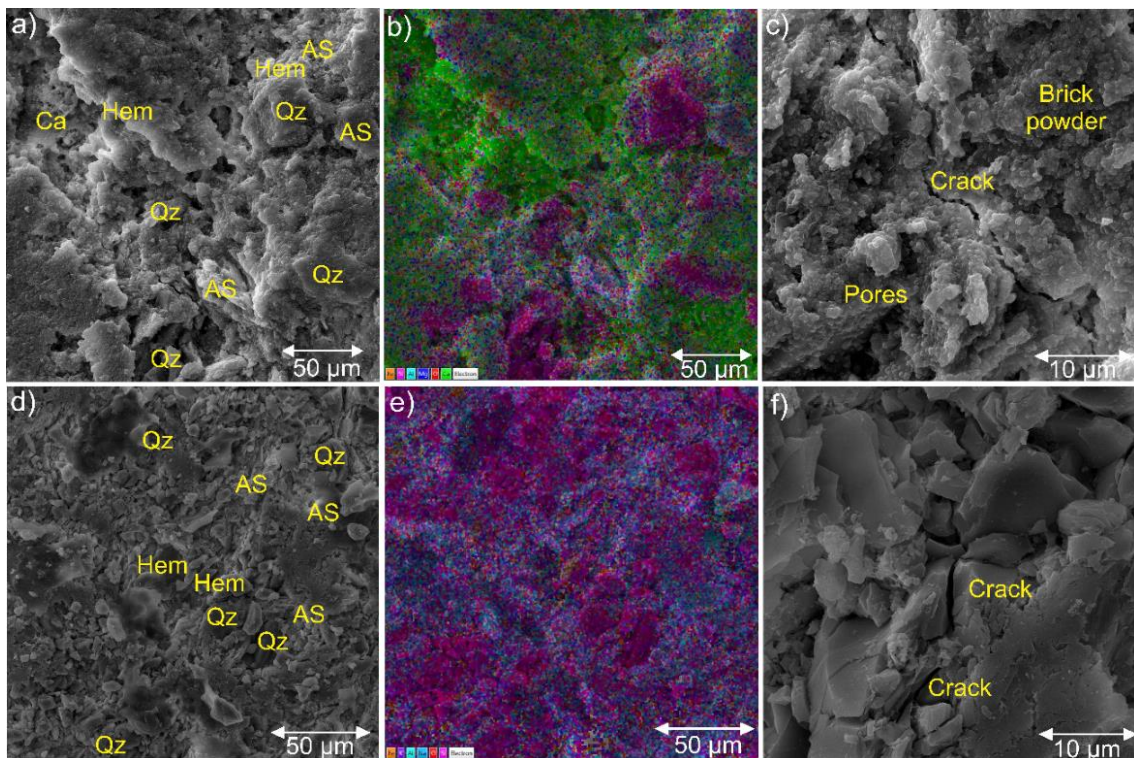


Figure 24. FE-SEM micrographs magnified to 1,000x (with EDS layered image) and 5,000x (50 µm and 10 µm). A-2-10 (a, b, and c) and A-2-10-A (d, e, and f). The used symbols are Qz – Quartz grains, AS – Aluminium silicate phase, Ca – calcium-bearing phase, and Hem – Hematite.

**Table 6. EDS analysis of the cement mortar R2**

Elements (Wt.%)	R2 (Figure 23-a)	R2 (Figure 23-c)	R2-A (Figure 23-d)	R2-A (Figure 23-f)
O	49.11	60.12	52.36	69.49
Na	0.70	0.59	0.39	0.36
Mg	0.75	0.60	0.77	0.67
Al	5.91	4.29	6.14	4.83
Si	14.62	10.19	16.21	12.25
S	0.28	0.17	0.81	0.53
Cl	-	-	0.25	0.15
K	1.41	0.70	1.29	0.70
Ca	14.55	7.11	18.16	9.62
Fe	3.11	1.09	3.62	1.37
Ti	0.16	0.16	-	-
C	9.18	14.94	-	-

**Table 7. EDS analysis of the alkali-activated mortar A-2-10**

Elements (Wt.%)	A-2-10 (Figure 24-a)	A-2-10 (Figure 24-c)	A-2-10-A (Figure 24-d)	A-2-10-A (Figure 24-f)
O	52.95	70.40	48.22	63.76
Na	0.32	0.29	2.37	2.18
Mg	0.93	0.82	0.70	0.61
Al	5.22	4.12	8.18	6.42
Si	14.52	10.99	27.80	20.94
S	0.54	0.36	-	-
Cl	0.13	0.08	-	-
K	0.96	0.52	6.66	3.60
Ca	20.82	11.05	1.07	0.57
Fe	3.61	1.37	4.39	1.66
Ti	-	-	0.60	0.27

#### 2.2.4. Discussion

Table 3 indicates that the crushed brick aggregate (CBA) and the brick powder (BP) are abundant in  $Al_2O_3$  and  $SiO_2$ , yet they exhibit low levels of CaO. In contrast, cement (CEM) shows a higher CaO content. Additionally, CBA and BP possess a greater proportion of  $Fe_2O_3$  compared to cement and demonstrate a lower loss on ignition than cement. Table 4 presents the values for  $D_{10}$  (the particle diameter at which less than 10% of all particles are smaller),  $D_{50}$  (the particle diameter at which 50% of all particles are smaller and 50% are larger),  $D_{90}$  (the particle diameter at which less than 90% of all particles are smaller),  $D_{modal}$  (the particle diameter corresponding to the peak point of the particle size distribution diagram),  $D_{mean}$  (the mean particle diameter), and the distribution range (the range of particle sizes). The data clearly indicate that CEM is the fines material, followed by BP, while CBA is the coarsest among the materials analyzed. The distribution range is calculated by subtracting the value of  $D_{10}$  from  $D_{90}$  and dividing the result by  $D_{50}$ . The smallest distribution range is observed for CBA, with CEM exhibiting the largest range.

The mineralogical analysis conducted through FT-IR on the initial materials (Figure 8) provided supplementary insights to the XRF results. The most prominent bands, located around  $1000\text{ cm}^{-1}$ , are characteristic of the aluminosilicates, indicating the asymmetric stretching vibrations of Si-O-Si and Si-O-Al [45]. Particularly, these bands are more pronounced in sample BP compared to sample CBA, reflecting a higher abundance of quartz and feldspars. Furthermore, the intensity of these bands tends to increase in powders with finer particle sizes [46]. The band found at  $691\text{-}692\text{ cm}^{-1}$  in fired BP samples reflect the bending vibration of crystalline quartz. Additionally, small doublets in both samples indicate stretching vibrations of an amorphous quartz component, detected around  $775\text{ cm}^{-1}$  [46]. This suggests that the material is partially crystallized and partially amorphous [32]. The lack of absorption bands in the range of  $3600\text{-}3700\text{ cm}^{-1}$  and approximately  $1640\text{ cm}^{-1}$  implied the absence or minimal presence of clay minerals in the waste brick [47-49]. Moreover, the characteristic wide band of asymmetric stretching of  $CaCO_3$  at approximately  $1458\text{ cm}^{-1}$  was not observed in samples BP and CBA, although it was clearly identified in the CEM sample [50]. Lastly, a band at  $554\text{-}556\text{ cm}^{-1}$ , indicative of trace amounts of hematite [32, 45], is more pronounced in BP than in CBA, aligning well with the findings from the XRF analysis.

A small band observed at  $1618\text{ cm}^{-1}$  in CEM is attributed to the bending vibration of water in sulfates [51]. The bands around  $513$  and  $881\text{ cm}^{-1}$  correspond to the bending-in-plane vibrations of Si-O bonds in Si-O-Si/Si-O-Al, while the asymmetric stretching vibration of the same bond is detected at  $1152\text{ cm}^{-1}$  [52]. Additionally, slightly noticeable bands between  $600$  and  $659\text{ cm}^{-1}$  indicate a bending vibration of Al-O in IV-fold coordination with a  $\text{SiO}_4$  [52].

As shown in Figure 9, the alkali-activated “lollipops” produced solely with KOH were prone to crumbling, in contrast to those made with a mixed solution of KOH and  $\text{Na}_2\text{SiO}_3$ , which exhibited a much more compact structure. Due to the disintegration of the alkali-activated “lollipops” made exclusively with KOH, these mixtures were excluded from further investigation.

A reduced number of surface cracks were observed in samples cured with metal plate coverage compared to those cured with foil coverage (see Figures 11-a and 11-c). Additionally, distortion was less pronounced in the samples cured with metal plate coverage (see Figures 11-b and 11-d). A comparison of Figures 12-c and 12-d with Figures 13-e and 13-f reveals that the alkali-activated mortar samples from series A2 exhibited fewer surface cracks than those from series A1, with distortion also being less evident in the samples from series A2. This suggests that a fluid consistency may contribute to the formation of surface cracks and distortion in the samples. Due to the high incidence of surface cracks and significant distortion, a portion of the A1 sample series, which was cured at elevated temperatures under foil coverage, was excluded from further testing. All alkali-activated mortar samples cured at elevated temperatures with metal plate coverage, along with the cement mortar samples, were subjected to high-temperature exposure as detailed below.

From Figure 14, it is evident that mortars with a plastic consistency (Figure 14-b) achieve higher flexural strength values compared to those with a fluid consistency (Figure 14-a). This outcome aligns with expectations, as a higher water/cement ratio, as observed in the A1 series mortars, typically leads to poorer mechanical properties [53]. Notably, the flexural strengths recorded after exposure to high temperatures were consistently lower than the initial values, with the exception of the A-2-10 mortar mix, which demonstrated an increase in flexural strength post-exposure. The higher residual flexural strength value for R1, in contrast to R2, contradicts the findings of Messaoudene et al. [54], who asserted that a higher water/cement ratio adversely affects the properties of cement mortar after high-temperature exposure more significantly than a lower water/cement ratio. Figure 15-a illustrates that fluid consistency cement mortar (R1) retains a greater percentage of residual flexural strength compared to the alkali-activated mortars (A1 series) following fire exposure. Conversely, Figure 15-b reveals that the alkali-activated mortars (A2 series) exhibit higher percentages of residual flexural strength than the cement mortar. Specifically, for the fluid consistency mortars (A1 series) after fire exposure, the retained percentages of initial flexural strength are as follows: 99% for mortar R1, 89.4% for mortar A-1-10, 62.2% for mortar A-1-12, and 63.1% for mortar A-1-14. In the case of plastic consistency mortars (A2 series), the residual strengths are 84.4% for mortar R2, 140.3% for mortar A-2-10, 98.1% for mortar A-2-12, and 71.2% for mortar A-2-14.

Plastic consistency mortars (Figure 16-b) achieve higher compressive strength values compared to fluid consistency mortars (Figure 16-a). This outcome is anticipated due to the elevated water/cement ratio present in the fluid consistency mortars (A1 series). Notably, compressive strengths following exposure to high temperatures were consistently lower than the initial values for the same property, with the exception of the A-2-10 mortar mix, which demonstrated an increase in compressive strength recorded in fire-exposed samples of alkali-activated composites, as reported by Abd Razak et al. [21]. Figures 17-a and 17-b reveal that the percentages of remaining compressive strength of alkali-activated mortar generally surpass those of cement mortar. However, A-1-14 stands out as an exception, exhibiting a slightly lower remaining compressive strength compared to its reference mix, R1. Specifically, for fluid consistency mortars, the retained percentages of initial compressive strength after firing were as follows: 82.3% for mortar R1, 99.5% for mortar A-1-10, 84.2% for mortar A-1-12, and 75.7% for mortar A-1-14. In contrast, the residual compressive strengths for plastic consistency mortars were 78.6% for mortar R2, 122.9% for mortar A-2-10, 110.1% for mortar A-2-12, and 84.3% for A-2-14. The higher remaining compressive strength of R1 compared to R2 contradicts the findings presented by Messaoudene et al. [54]. For alkali-activated mortars, those with a lower proportion of the liquid component (plastic consistency mortars) demonstrated enhanced remaining compressive strength values relative to those with a higher liquid component proportion (fluid consistency mortars) at the same alkali activator concentration, aligning with the results reported by Palizi & Toufigh [55]. The more significant strength reduction observed in cement mortar compared to alkali-activated mortars can be attributed to the substantial presence of calcite and calcium hydroxide in Portland cement, which decompose at temperatures reaching up to  $600^\circ\text{C}$ . This is further influenced by the lower quantities of calcite and calcium hydroxide found in alkali-activated binders [19]. The strength increase noted in alkali-activated mortars is explained by Pan et al. [19] as being due to the formation of a geopolymeric gel. This gel fills the matrix, making it denser and positively affecting the strength.

The insights regarding the absolute values of flexural and compressive strengths of mortars also extend to the elasticity moduli. Mortars with plastic consistency (Figure 18-b) demonstrate higher elasticity moduli compared to those with fluid consistency (Figure 18-a). Notably, the elasticity moduli values after exposure to high temperature are

consistently lower than the initial values, with the exception of the A-2-10 mortar mix, which exhibited an increase in the elasticity moduli post-exposure. This increase aligns with findings reported by Pan et al. [17]. Figure 19 indicates that all alkali-activated mortars in both series outperform cement mortars in terms of remaining elasticity moduli. Among alkali-activated mortars, those with a lower liquid component proportion (plastic consistency) show superior remaining elasticity moduli compared to those with a higher liquid component proportion (fluid consistency) at the same alkali activator concentration, corroborating the results presented by Palizi & Toufigh [55]. The remaining elasticity moduli percentages for mortars in series A-1 are as follows: 77.9% for mortar R1, 94.9% for mortar A-1-10, 90.9% for mortar A-1-12, and 98.9% for mortar A-1-14. For series A-2, the percentages are 81.9% for mortar R2, 114.3% for mortar A-2-10, 94.6% for mortar A-2-12, and 85% for mortar A-2-14.

Figure 20 reveals that cement mortars experience a higher mass loss compared to alkali-activated mortar mixtures [20-22], irrespective of their consistency. This mass loss for cement mortars from both series is recorded at 3.9%, while alkali-activated mortars exhibit a narrower mass loss range of 2.5% to 2.7% (Figure 20). Although this study did not assess samples at a temperature of 400 °C, Duan et al. [22] noted that at this temperature, mass losses due to the firing of Portland cement composites and alkali-activated composites become equivalent. Beyond this temperature threshold, the mass of alkali-activated composites remains relatively stable with increasing temperature, whereas the mass of Portland cement composites significantly decreases up to 600 °C, at which point monitoring becomes impossible due to the sample decomposition.

Figure 21 shows that both cement mortars and alkali-activated mortars underwent a color change following exposure to high temperatures. Additionally, the alkali-activated mortars developed cracks in their cross-section when subjected to elevated temperatures, with a notably higher number of cracks observed in the fluid consistency alkali-activated mortar (Figure 21-f) compared to the plastic consistency variant (Figure 21-h). This observation accounts for the greater retention of properties in mortar A-2-10 after high-temperature exposure, in contrast to mortar A-1-10. At the magnification used, no visible cracks were observed in mortars R1 and R2 post-exposure (Figures 21-b and 21-d). As noted by Alshuqari & Cevik [56], thermal stresses induced by the evaporation of water from the alkali-activated matrix during heating can lead to cracking. Given that the fluid-consistency mortar contains a higher water content than its plastic-consistency counterpart, this explanation corroborates the increased number of cracks observed in the fluid-consistency alkali-activated mortar during firing compared to the plastic-consistency variant.

The FT-IR spectra of the alkali-activated materials (Figure 22) revealed significant bands corresponding to feldspars in fired ceramic materials and quartz in all the tested mortars, located between 988 and 998  $\text{cm}^{-1}$ . The sharpest and most pronounced band was identified in sample A-2-10, likely due to the lower quantity of geopolymers that occurred. The shift of this critical band to lower wave numbers compared to the initial materials is thought to signify the activation mechanism that facilitates the development of a substantial amorphous phase [34]. Based on the position of this band, the most effectively activated material was A-2-10-A. The bands observed at 692-694  $\text{cm}^{-1}$  correspond to the bending vibrations of crystalline quartz [34], primarily sourced from waste bricks. The bands recorded in the R2 and R2-A samples at 874 and 1417  $\text{cm}^{-1}$  (but not in the A samples) are attributed to carbonates [57]. A minimal amount of hematite was detected at 520-561  $\text{cm}^{-1}$  [34, 45], with the highest concentration found in sample A-2-10, which was tested at room temperature. The presence of a metal plate may have slowed down certain reactions during curing, while subsequent conditions could have triggered additional hematite reactions. Very subtle bands in the 644-648  $\text{cm}^{-1}$  range indicated Al-O bending vibrations [52].

The calcium-bearing phase visible in Figure 23-a is likely attributed to C-S-H, CH, and  $\text{CaCO}_3$  in mortar R2. Notably, calcium-bearing phases remain present even after exposing mortar R2 to a temperature of 600 °C (Figure 23-d), aligning with the findings of Vetter et al. [58], who reported that these phases completely decompose at 740 °C. In the R2 samples, iron is uniformly distributed, likely originating from CBA, as shown in Figures 23a and 23d.

Quartz and hematite, identified in the R2 mortar sample at room temperature (Figure 23-a) and derived from crushed brick aggregate, decompose at temperatures of 573 °C [59] and above 1300 °C [60]. Consequently, these minerals can still be detected in the R2 mortar sample even after exposure to high temperatures (Figure 23-d). An aluminosilicate phase was identified in the R2 mortar sample at room temperature but was absent at elevated temperatures. The images of the mortar samples, both before (Figure 23-b) and after (Figure 23-e) exposure to high temperatures, reveal a composition primarily consisting of silicon and calcium, followed by aluminum, iron, and some potassium, a finding corroborated by EDS analysis (Table 6). The EDS analysis indicates the presence of carbon in the sample prior to high-temperature exposure, but not afterwards (Table 6). This suggests that during high-temperature exposure,  $\text{CaCO}_3$  decomposed into CaO and  $\text{CO}_2$ , with the latter dissipating. The decomposition of  $\text{CaCO}_3$  was detected before reaching 700 °C, as noted by Karunadasa et al. [61]. Figures 23-c and 24-c illustrate cracks in both alkali-activated and Portland cement mortar samples, likely resulting from drying shrinkage [62]. However, the crack in Figure 23-c appears narrower than in Figure 24-c, supporting the findings of Wei et al. [38], who observed that alkali-activated mortars typically experience greater shrinkage than Portland cement mortars, leading to wider cracks. The formation of cracks due to drying can be mitigated by incorporating fibers into the alkali-activated composite mixture [63]. Although the crack was present in the Portland cement mortar before firing, it was not observed in the sample after firing (Figure 23-f).

Calcium-bearing phases, quartz, and hematite are prominently observed in the images of the alkali-activated mortar sample A-2-10, both prior to (Figure 24-a) and following high-temperature exposure (Figure 24-d). In contrast to the R2 sample, this mortar incorporates aluminosilicate phases before and after exposure to elevated temperatures, likely in the form of mullite, which exhibits high thermal stability and only decomposes at temperatures exceeding 1000°C [14]. The presence of silicon and aluminum is evident in Figure 24b and confirmed by EDS analysis in Table 7. Notably, the quantities of silicon and aluminum are seen in Figure 24-b and corroborated by EDS analysis in Table 7. The quantities of silicon and aluminum in the fired samples have nearly doubled. Calcium, which is present at room temperature (Figure 24-b and Table 7), has significantly diminished post-firing, while the proportion of potassium (Figure 24-b) has markedly increased. These EDS analysis results indicate the formation of an N-A-S-H gel, specifically its K-A-S-H variant, which remains stable at high temperatures [10]. According to Song et al. [23], N-A-S-H and K-A-S-H gels decompose only at temperatures of 800°C and 1200°C, respectively, which explains the alkali-activated mortar's impressive mechanical properties post-firing. A comparison of Figures 24-c and 24-f reveals that as the temperature rises, the mortar's structure becomes increasingly densified, aligning with the findings of Duan et al. [22] and Song et al. [23]. The densification may result from the sintering and melting processes of alkali-activated mortars, which initiate at temperatures around 600 °C [64].

According to Song et al. [23], densification can lead to the formation of microcracks in alkali-activated mortar, as illustrated in Figure 24c. Figure 24-f not only depicts a crack but also indicates a reduced pore content within the mortar. This crack may result from thermal stress due to water evaporation from the alkali-activated matrix during heating [56].

Sandeep et al. [5] emphasize that the Si/Al ratio is crucial in determining the mechanical properties retained after exposure to high temperatures. Higher Si/Al ratios correlate with improved residual properties of the composite. The EDS analysis results of Portland cement mortar prior to high-temperature exposure (as shown in the 2nd and 3rd columns of Table 6) reveal Si/Al ratios of 2.47 and 2.4. In contrast, the EDS analysis of alkali-activated mortar before exposure (2nd and 3rd columns of Table 7) shows Si/Al ratios of 2.78 and 2.66. As previously illustrated in Figures 15-b, 17-b, and 19-b, the alkali-activated mortar A-2-10 demonstrated superior residual properties compared to the Portland cement mortar R2, attributable to its higher Si/Al ratio.

The alkali-activated mortars examined in this study demonstrated enhanced performance in withstanding high temperatures compared to traditional cement mortars. These mortars have potential applications in the fabrication of protective boards for materials such as structural steel or wood, thereby extending the duration these structures can support loads during a fire. Ongoing research in this field aims to achieve similar properties in alkali-activated mortars while streamlining their preparation process. This includes utilizing the heat generated during the preparation of alkali-activated solutions to facilitate the internal curing of the mortars.

### 3. Conclusion

This paper explores the fire resistance of alkali-activated mortars composed entirely of bricks, with the objective of evaluating the benefits of utilizing crushed brick waste. Two series of mortars were produced, differing in workability: one series of cement mortar and three series of alkali-activated mortars, each with varying molarities of KOH solution (10, 12, and 14 M).

The findings indicate that using KOH solution exclusively as an alkali activator results in the instability of alkali-activated mortars, leading to their decomposition upon contact with water. In contrast, the combination of KOH solution and Na<sub>2</sub>SiO<sub>3</sub> as activators yields stable samples. Consequently, subsequent research and conclusions concentrate on alkali-activated mortars that incorporate KOH solution at different molarities and Na<sub>2</sub>SiO<sub>3</sub> as the alkaline activator.

At room temperature, the mechanical properties of cement mortars surpass those of any alkali-activated mortars, irrespective of their workability. However, after exposure to high temperatures, alkali-activated mortars with plastic consistency consistently retain a greater percentage of their mechanical properties and exhibit lower mass loss compared to cement mortars. Similarly, alkali-activated mortars with fluid consistency generally demonstrate higher retained mechanical properties and lower mass loss after high-temperature exposure than cement mortar. The slightly diminished properties in fluid-consistency alkali-activated mortars, relative to cement mortar, can be attributed to the increased formation of cracks during firing. These cracks are directly related to thermal stresses caused by the evaporation of water from the alkali-activated matrix during heating. The superior fire resistance of alkali-activated mortars compared to cement mortars is likely due to the formation of mullite and N-A-S-H (K-A-S-H) gel in the alkali-activated matrix.

The most effective fire resistance, characterized by the highest remaining mechanical properties and lowest mass loss after firing, was observed in the plastic consistency alkali-activated mortar made with a 10 molar KOH solution and Na<sub>2</sub>SiO<sub>3</sub>. This type of alkali-activated mortar shows promise for application in fire protection boards for buildings, and the incorporation of crushed brick waste in such applications would enhance the value of this material.

## 4. Declarations

### 4.1. Author Contributions

Conceptualization, D.K.; methodology, D.K., I.N.G., and M.V.V.; formal analysis, D.K.; investigation, D.K., R.R., N.M., and M.V.V.; resources, I.N.G. and N.T.; writing—original draft preparation, D.K. and M.V.V.; writing—review and editing, D.K., I.N.G., N.T., R.R., N.M., and M.V.V.; visualization, D.K. and M.V.V.; supervision, I.N.G. and N.T. All authors have read and agreed to the published version of the manuscript.

### 4.2. Data Availability Statement

The data presented in this study are available on request from the corresponding author.

### 4.3. Funding

The results presented in this scientific paper have been obtained through the research activities within the project “Sustainable Building Composites” of University North, Croatia. The authors are also thankful for the support of the Ministry of Science, Technological Development and Innovation of the Republic of Serbia, Contract No. 451-03-66/2024-03/200012 as well as for the support of the European Cooperation in Science and Technology through COST Action CA20133.

### 4.4. Acknowledgements

The authors would like to express their sincere gratitude to the Faculty of Technology and Metallurgy, University of Belgrade for providing the Field Emission Scanning Electron Microscopy equipped with Energy Dispersive Spectroscopy (FE-SEM-EDS) screening that significantly contributed to this research. Their support and expertise were invaluable in achieving the results presented in this paper.

### 4.5. Conflicts of Interest

The authors declare no conflict of interest.

## 5. References

- [1] Malik, M., Bhattacharyya, S. K., & Barai, S. V. (2021). Thermal and mechanical properties of concrete and its constituents at elevated temperatures: A review. *Construction and Building Materials*, 270, 121398. doi:10.1016/j.conbuildmat.2020.121398.
- [2] Netinger, I., Rukavina, M. J., & Mladenović, A. (2013). Improvement of post-fire properties of concrete with steel slag aggregate. *Procedia Engineering*, 62, 745–753. doi:10.1016/j.proeng.2013.08.121.
- [3] Gökçe, H. S. (2024). Durability of slag-based alkali-activated materials: A critical review. *Journal of the Australian Ceramic Society*, 60(3), 885–903. doi:10.1007/s41779-024-01011-z.
- [4] Ghazy, M. F., Metwally Abd Allah, A. B. D., Taman, M., & Mehriz, A. (2023). Performance of geopolymers mortars prepared by different alkaline solutions under elevated temperature. *Journal of Materials and Engineering Structures*, 10(3), 423–447.
- [5] Sandeep, G. S., Pandit, P., Prashanth, S., & Jagadisha, H. M. (2024). Influence of Gypsum on the Residual Properties of Fly Ash-Slag-Based Alkali-Activated Concrete. *Civil Engineering Journal (Iran)*, 10(3), 915–927. doi:10.28991/CEJ-2024-010-03-017.
- [6] Provis, J. L. (2018). Alkali-activated materials. *Cement and Concrete Research*, 114, 40–48. doi:10.1016/j.cemconres.2017.02.009.
- [7] Kravchenko, E., Lazorenko, G., Jiang, X., & Leng, Z. (2024). Alkali-activated materials made of construction and demolition waste as precursors: A review. *Sustainable Materials and Technologies*, 39, 829. doi:10.1016/j.susmat.2024.e00829.
- [8] Jamalimoghadam, M., Vakili, A. H., Keskin, I., Totonchi, A., & Bahmyari, H. (2024). Solidification and utilization of municipal solid waste incineration ashes: Advancements in alkali-activated materials and stabilization techniques, a review. *Journal of Environmental Management*, 367, 122014. doi:10.1016/j.jenvman.2024.122014.
- [9] Leng, Z., Caon, Y., Zhu, X., Christou, G., Li, S., Mohd, N. A., & El Atar, S. (2024). From Debris to Innovation: Unveiling a New Frontier for Alkali-Activated Materials. *Journal of Cleaner Production*, 143218, 143218. doi:10.1016/j.jclepro.2024.143218.
- [10] Shaikh, F. U. A., Kahlon, N. S., & Dogar, A. U. R. (2023). Effect of Elevated Temperature on the Behavior of Amorphous Metallic Fibre-Reinforced Cement and Geopolymer Composites. *Fibers*, 11(4), 31. doi:10.3390/fib11040031.
- [11] Sedira, N., Castro-Gomes, J., & Magrinho, M. (2018). Red clay brick and tungsten mining waste-based alkali-activated binder: Microstructural and mechanical properties. *Construction and Building Materials*, 190, 1034–1048. doi:10.1016/j.conbuildmat.2018.09.153.
- [12] da Costa Gonçalves, L. F., Balestra, C. E. T., & Ramirez Gil, M. A. (2023). Evaluation of mechanical, physical and chemical properties of ecological modular soil-alkali activated bricks without Portland cement. *Environmental Development*, 48, 100932. doi:10.1016/j.envdev.2023.100932.

- [13] Li, Z., Xu, G., & Shi, X. (2021). Reactivity of coal fly ash used in cementitious binder systems: A state-of-the-art overview. *Fuel*, 301, 121031. doi:10.1016/j.fuel.2021.121031.
- [14] Seyedian Choubi, S., & Meral Akgul, C. (2022). High temperature exposure of alkali-activated coal fly ashes. *Journal of Building Engineering*, 59, 105081. doi:10.1016/j.job.2022.105081.
- [15] Tran, N. P., Nguyen, T. N., Black, J. R., & Ngo, T. D. (2024). High-temperature stability of ambient-cured one-part alkali-activated materials incorporating graphene nanoplatelets for thermal energy storage. *Developments in the Built Environment*, 18, 100447. doi:10.1016/j.dibe.2024.100447.
- [16] Statkauskas, M., Vaičiukynienė, D., Grinys, A., & Paul Borg, R. (2023). Mechanical properties and microstructure of ternary alkali activated system: Red brick waste, metakaolin and phosphogypsum. *Construction and Building Materials*, 387, 131648. doi:10.1016/j.conbuildmat.2023.131648.
- [17] Pan, Z., Sanjayan, J. G., & Collins, F. (2014). Effect of transient creep on compressive strength of geopolymer concrete for elevated temperature exposure. *Cement and Concrete Research*, 56, 182–189. doi:10.1016/j.cemconres.2013.11.014.
- [18] Abdulmatin, A., Sa, N., Dueramae, S., Haruehansapong, S., Tangchirapat, W., & Jaturapitakkul, C. (2024). Strength and Acid Resistance of Mortar with Different Binders from Palm Oil Fuel Ash, Slag, and Calcium Carbide Residue. *Civil Engineering Journal (Iran)*, 10(7), 2195–2215. doi:10.28991/CEJ-2024-010-07-08.
- [19] Pan, Z., Tao, Z., Cao, Y. F., Wuhner, R., & Murphy, T. (2018). Compressive strength and microstructure of alkali-activated fly ash/slag binders at high temperature. *Cement and Concrete Composites*, 86, 9–18. doi:10.1016/j.cemconcomp.2017.09.011.
- [20] Jiang, X., Xiao, R., Zhang, M., Hu, W., Bai, Y., & Huang, B. (2020). A laboratory investigation of steel to fly ash-based geopolymer paste bonding behavior after exposure to elevated temperatures. *Construction and Building Materials*, 254, 119267. doi:10.1016/j.conbuildmat.2020.119267.
- [21] Abd Razak, S. N., Shafiq, N., Guillaumat, L., Farhan, S. A., & Lohana, V. K. (2022). Fire-Exposed Fly-Ash-Based Geopolymer Concrete: Effects of Burning Temperature on Mechanical and Microstructural Properties. *Materials*, 15(5), 1884. doi:10.3390/ma15051884.
- [22] Duan, P., Yan, C., Zhou, W., & Luo, W. (2015). Thermal Behavior of Portland Cement and Fly Ash–Metakaolin-Based Geopolymer Cement Pastes. *Arabian Journal for Science and Engineering*, 40(8), 2261–2269. doi:10.1007/s13369-015-1748-0.
- [23] Song, Q., Guo, M. Z., & Ling, T. C. (2022). A review of elevated-temperature properties of alternative binders: Supplementary cementitious materials and alkali-activated materials. *Construction and Building Materials*, 341, 127894. doi:10.1016/j.conbuildmat.2022.127894.
- [24] Gado, R. A., Hebda, M., Lach, M., & Mikula, J. (2020). Alkali activation of waste clay bricks: Influence of the silica modulus, SiO<sub>2</sub>/Na<sub>2</sub>O, H<sub>2</sub>O/Na<sub>2</sub>O molar ratio, and liquid/solid ratio. *Materials*, 13(2), 383. doi:10.3390/ma13020383.
- [25] Cardoza, A., & Colorado, H. A. (2023). Alkali-activated cement manufactured by the alkaline activation of demolition and construction waste using brick and concrete wastes. *Open Ceramics*, 16, 100438. doi:10.1016/j.oceram.2023.100438.
- [26] García-Díaz, A., Delgado-Plana, P., Bueno-Rodríguez, S., & Eliche-Quesada, D. (2024). Investigation of waste clay brick (chamotte) addition and activator modulus in the properties of alkaline activation cements based on construction and demolition waste. *Journal of Building Engineering*, 84, 108568. doi:10.1016/j.job.2024.108568.
- [27] Robayo, R. A., Mulford, A., Munera, J., & Mejía de Gutiérrez, R. (2016). Alternative cements based on alkali-activated red clay brick waste. *Construction and Building Materials*, 128, 163–169. doi:10.1016/j.conbuildmat.2016.10.023.
- [28] Robayo-Salazar, R. A., Mejía-Arcila, J. M., & Mejía de Gutiérrez, R. (2017). Eco-efficient alkali-activated cement based on red clay brick wastes suitable for the manufacturing of building materials. *Journal of Cleaner Production*, 166, 242–252. doi:10.1016/j.jclepro.2017.07.243.
- [29] Zhang, Z., Wong, Y. C., & Arulrajah, A. (2021). Feasibility of producing non-fired compressed masonry units from brick clay mill residues by alkali activation. *Journal of Cleaner Production*, 306, 126916. doi:10.1016/j.jclepro.2021.126916.
- [30] Ulugöl, H., Kul, A., Yıldırım, G., Şahmaran, M., Aldemir, A., Figueira, D., & Ashour, A. (2021). Mechanical and microstructural characterization of geopolymers from assorted construction and demolition waste-based masonry and glass. *Journal of Cleaner Production*, 280, 124358. doi:10.1016/j.jclepro.2020.124358.
- [31] Yıldırım, G., Kul, A., Özçelikci, E., Şahmaran, M., Aldemir, A., Figueira, D., & Ashour, A. (2021). Development of alkali-activated binders from recycled mixed masonry-originated waste. *Journal of Building Engineering*, 33, 101690. doi:10.1016/j.job.2020.101690.
- [32] Vasić, M. V., Terzić, A., Radovanović, Ž., Radojević, Z., & Warr, L. N. (2022). Alkali-activated geopolymerization of a low illitic raw clay and waste brick mixture. An alternative to traditional ceramics. *Applied Clay Science*, 218, 106410. doi:10.1016/j.clay.2022.106410.

- [33] Reig, L., Tashima, M. M., Borrachero, M. V., Monzó, J., Cheeseman, C. R., & Payá, J. (2013). Properties and microstructure of alkali-activated red clay brick waste. *Construction and Building Materials*, 43, 98–106. doi:10.1016/j.conbuildmat.2013.01.031.
- [34] Tuyan, M., Andiç-Çakir, Ö., & Ramyar, K. (2018). Effect of alkali activator concentration and curing condition on strength and microstructure of waste clay brick powder-based geopolymer. *Composites Part B: Engineering*, 135, 242–252. doi:10.1016/j.compositesb.2017.10.013.
- [35] Hosan, A., Haque, S., & Shaikh, F. (2016). Compressive behaviour of sodium and potassium activators synthesized fly ash geopolymer at elevated temperatures: A comparative study. *Journal of Building Engineering*, 8, 123–130. doi:10.1016/j.jobe.2016.10.005.
- [36] Fernández-Jiménez, A., Palomo, A., & Criado, M. (2006). Alkali activated fly ash binders. A comparative study between sodium and potassium activators. *Materiales de Construcción*, 56(281), 51–65. doi:10.3989/mc.2006.v56.i281.92.
- [37] Gil, A., Banerji, S., & Kodur, V. (2023). Factors influencing pore pressure measurements in concrete during heating and its influence on fire-induced spalling. *Cement and Concrete Composites*, 142, 105228. doi:10.1016/j.cemconcomp.2023.105228.
- [38] Lahoti, M., Wijaya, S. F., Tan, K. H., & Yang, E. H. (2020). Tailoring sodium-based fly ash geopolymers with variegated thermal performance. *Cement and Concrete Composites*, 107, 103507. doi:10.1016/j.cemconcomp.2019.103507.
- [39] Fernandes, F. M., Lourenço, P. B., & Castro, F. (2010). Ancient Clay Bricks: Manufacture and Properties. *Materials, Technologies and Practice in Historic Heritage Structures*, 1(3), 29–48. doi:10.1007/978-90-481-2684-2\_3.
- [40] EN 196-2:2013. (2013). Methods of testing cement - Part 2: Chemical analysis of cement. European Committee for Standardization, Brussels, Belgium.
- [41] ISO 13320:2020. (2020). Particle size analysis - Laser diffraction methods. International Organization for Standardization (ISO), Geneva, Switzerland.
- [42] EN 1015-3:1999. (1999). Methods of test for mortar for masonry - Part 3: Determination of consistence of fresh mortar. European Committee for Standardization, Brussels, Belgium.
- [43] RILEM TC 129-MHT. (2004). Test methods for mechanical properties of concrete at high temperatures: Modulus of elasticity for service and accident conditions. *Materials and Structures*, 37(266), 139–144.
- [44] EN 1015-11:2019 (2019). Methods of test for mortar for masonry - Part 11: Determination of flexural and compressive strength of hardened mortar. European Committee for Standardization, Brussels, Belgium.
- [45] Kumar Mishra, A., Mishra, A., & Anshumali. (2021). Geochemical characterization of bricks used in historical monuments of 14-18th century CE of Haryana region of the Indian subcontinent: Reference to raw materials and production technique. *Construction and Building Materials*, 269, 121802. doi:10.1016/j.conbuildmat.2020.121802.
- [46] Hlavay, J., Jonas, K., Elek, S., & Inczedy, J. (1978). Characterization of the Particle Size and the Crystallinity of Certain Minerals by Ir Spectrophotometry and Other Instrumental Methods - 2. Investigations on Quartz and Feldspar. *Clays and Clay Minerals*, 26(2), 139–143. doi:10.1346/CCMN.1978.0260209.
- [47] Agrawal, P., & Misra, S. N. (2014). Irreversible Dilatometry as a Tool for Body Composition and Firing Schedule Design in Traditional Ceramics. *Transactions of the Indian Ceramic Society*, 73(1), 14–21. doi:10.1080/0371750X.2013.870049.
- [48] Prud'homme, E., Michaud, P., Joussein, E., Peyratout, C., Smith, A., & Rossignol, S. (2011). In situ inorganic foams prepared from various clays at low temperature. *Applied Clay Science*, 51(1–2), 15–22. doi:10.1016/j.clay.2010.10.016.
- [49] Vasić, M. V., Jantunen, H., Mijatović, N., Nelo, M., & Muñoz Velasco, P. (2023). Influence of coal ashes on fired clay brick quality: Random forest regression and artificial neural networks modeling. *Journal of Cleaner Production*, 407, 137153. doi:10.1016/j.jclepro.2023.137153.
- [50] Peyne, J., Gautron, J., Doudeau, J., Joussein, E., & Rossignol, S. (2017). Influence of calcium addition on calcined brick clay based geopolymers: A thermal and FTIR spectroscopy study. *Construction and Building Materials*, 152, 794–803. doi:10.1016/j.conbuildmat.2017.07.047.
- [51] Santos, V. H. J. M. dos, Pontin, D., Ponzi, G. G. D., Stepanha, A. S. de G. e., Martel, R. B., Schütz, M. K., Einloft, S. M. O., & Dalla Vecchia, F. (2021). Application of Fourier Transform infrared spectroscopy (FTIR) coupled with multivariate regression for calcium carbonate (CaCO<sub>3</sub>) quantification in cement. *Construction and Building Materials*, 313, 125413. doi:10.1016/j.conbuildmat.2021.125413.
- [52] Yusuf, M. O. (2023). Bond Characterization in Cementitious Material Binders Using Fourier-Transform Infrared Spectroscopy. *Applied Sciences (Switzerland)*, 13(5), 3353. doi:10.3390/app13053353.
- [53] Li, X., Gu, X., Xia, X., Madenci, E., Chen, X., & Zhang, Q. (2022). Effect of water-cement ratio and size on tensile damage in hardened cement paste: Insight from peridynamic simulations. *Construction and Building Materials*, 356, 129256. doi:10.1016/j.conbuildmat.2022.129256.

- [54] Messaoudene, I., Ezziane, M., Lahouassa, A., Kaaloul, S., & Molez, L. (2021). Physico-mechanical and microstructural effects of water/cement ratio on the mortars upon heating. *Journal of Materials and Engineering Structures*, 8(2), 279-286.
- [55] Palizi, S., & Toufigh, V. (2023). Fire-induced damage assessment of cementless alkali-activated slag-based concrete. *Construction and Building Materials*, 393, 132002. doi:10.1016/j.conbuildmat.2023.132002.
- [56] Alshuqari, E. A., & Çevik, A. (2024). Bond-Slippage Characteristics between Carbon Fiber Reinforced Polymer Sheet and Heat-Damaged Geopolymer Concrete. *Civil Engineering Journal (Iran)*, 10(7), 2105–2122. doi:10.28991/CEJ-2024-010-07-03.
- [57] Hassaan, M. Y., & Abdel-Hakeem, N. (1989). Study of anhydrous and hydrated Portland cement containing alkali ions by infrared spectroscopy. *Journal of Materials Science Letters*, 8(5), 578–580. doi:10.1007/BF00720305.
- [58] Vetter, M., Gonzalez-Rodriguez, J., Nauha, E., & Kerr, T. (2019). The use of Raman spectroscopy to monitor phase changes in concrete following high temperature exposure. *Construction and Building Materials*, 204, 450–457. doi:10.1016/j.conbuildmat.2019.01.165.
- [59] Ismail Ahmed Ali, S., & Lublóy, E. (2022). Effect of elevated temperature on the magnetite and quartz concrete at different W/C ratios as nuclear shielding concretes. *Nuclear Materials and Energy*, 33, 101234. doi:10.1016/j.nme.2022.101234.
- [60] Wang, G., Zhang, J., Wang, Y., Tan, Y., Li, Z., Zhang, B., & Liu, Z. (2023). Study on the Bath Smelting Reduction Reaction and Mechanism of Iron Ore: A Review. *Metals*, 13(4), 672. doi:10.3390/met13040672.
- [61] Karunadasa, K. S. P., Manoratne, C. H., Pitawala, H. M. T. G. A., & Rajapakse, R. M. G. (2019). Thermal decomposition of calcium carbonate (calcite polymorph) as examined by in-situ high-temperature X-ray powder diffraction. *Journal of Physics and Chemistry of Solids*, 134, 21–28. doi:10.1016/j.jpcs.2019.05.023.
- [62] Hojati, M., Rajabipour, F., & Radlińska, A. (2019). Drying shrinkage of alkali-activated cements: effect of humidity and curing temperature. *Materials and Structures/Materiaux et Constructions*, 52(6), 118. doi:10.1617/s11527-019-1430-1.
- [63] Frayyeh, Q. J., & Kamil, M. H. (2021). The effect of adding fibers on dry shrinkage of geopolymer concrete. *Civil Engineering Journal (Iran)*, 7(12), 2099–2108. doi:10.28991/cej-2021-03091780.
- [64] Hager, I., Sitarz, M., & Mróz, K. (2021). Fly-ash based geopolymer mortar for high-temperature application – Effect of slag addition. *Journal of Cleaner Production*, 316, 128168. doi:10.1016/j.jclepro.2021.128168.